

Suppression of p -Wave Altermagnetism by Localized $4f$ Electrons in CeNiAsO

Jiuxiang Zhang^{1,2,‡}, Yueyang Sun^{1,2,3,‡}, Honglin Zhou^{1,2,‡}, Jumin Shi^{1,2,‡}, Di Wu^{1,2}, Hongze Gu^{1,2}, Wenjin Mao^{1,2}, Hengrui Dong^{1,2}, Yu Xu^{1,2}, Yinghao Li^{1,2}, Ziling Cao^{1,2}, Taimin Miao^{1,2}, Bo Liang^{1,2}, Neng Cai^{1,2}, Wenpei Zhu^{1,2}, Mingkai Xu^{1,2}, Jiaqi Chen^{1,2}, Chunhong Deng^{1,2}, Bo Liu^{1,2}, Xun Ma⁴, Zhengtai Liu^{5,6}, Mao Ye⁵, Shenjin Zhang⁷, Zhimin Wang⁷, Fengfeng Zhang⁷, Feng Yang⁷, Qinjun Peng⁷, Zuyan Xu⁷, Guodong Liu^{1,2,8}, Xintong Li^{1,2,8}, Hanqing Mao^{1,2,8}, Shiliang Li^{1,2,*}, Hongming Weng^{1,2,3,*}, Lin Zhao^{1,2,8,*} and X. J. Zhou^{1,2,8,*}

¹*Beijing National Laboratory for Condensed Matter Physics,
Institute of Physics, Chinese Academy of Sciences, Beijing 100190, China*

²*University of Chinese Academy of Sciences, Beijing 100049, China*

³*Condensed Matter Physics Data Center of Chinese
Academy of Sciences, Beijing 100190, China*

⁴*School of Nuclear Science and Technology,
University of Science and Technology of China, Hefei 230026, China*

⁵*Shanghai Synchrotron Radiation Facility,
Shanghai Advanced Research Institute,
Chinese Academy of Sciences, Shanghai 201210, China*

⁶*National Key Laboratory of Materials for Integrated Circuits,
Shanghai Institute of Microsystem and Information Technology,
Chinese Academy of Sciences, Shanghai 200050, China*

⁷*Technical Institute of Physics and Chemistry,
Chinese Academy of Sciences, Beijing, China*

⁸*Songshan Lake Materials Laboratory, Dongguan 523808, China*

[‡]*These people contributed equally to the present work.*

^{*}*Corresponding authors: slli@iphy.ac.cn,
hmweng@iphy.ac.cn, LZhao@iphy.ac.cn, XJZhou@iphy.ac.cn*

(Dated: June 2, 2026)

Altermagnetism, characterized by momentum-dependent spin splitting and zero net magnetization, has so far been explored mainly in weakly or moderately correlated d -electron systems. How such symmetry-allowed band splitting manifests in heavy-fermion materials, where magnetic exchange competes with Kondo correlations, remains unclear. Here we use high-resolution angle-resolved photoemission spectroscopy to investigate CeNiAsO, a heavy-fermion candidate for p -wave altermagnetism. Despite macroscopic signatures consistent with the proposed p -wave magnetic order, we find no resolvable near-Fermi-level p -wave exchange splitting on the Ni $3d$ -derived conduction bands across the Néel transitions. Fermi-surface mapping, orbital-resolved ARPES identify that the low-energy electronic structure is dominated by Ni $3d$ bands, while resonant photoemission reveals that the Ce $4f$ states remain predominantly localized with residual c - f hybridization. First-principles calculations further show that an uncorrected itinerant- $4f$ description produces dispersive Ce $4f$ bands and additional Fermi-surface pockets that are absent in experiment, thereby overestimating both the low-energy c - f hybridization and the exchange splitting transferred to the Ni $3d$ bands. When the localized Ce $4f$ character is incorporated through DFT+ U , the experimental Fermi-surface topology is recovered and the residual p -wave splitting on the Ni $3d$ -derived bands is reduced to only a few meV, below the effective experimental resolution. These results identify CeNiAsO as a strongly correlated f -electron limit of p -wave magnetism, in which localized $4f$ electrons suppress the observable single-particle band-splitting signature expected from a weak-correlation picture.

Introduction

Altermagnetism has recently broadened the classification of long-range magnetic order beyond the conventional ferromagnetic and antiferromagnetic dichotomy[1–3]. In the spin-space-group description, opposite-spin sublattices are connected by a real-space rotation or mirror operation rather than by a simple translation or inversion [4, 5]. This symmetry relation allows momentum-dependent, non-relativistic spin splitting of electronic bands even in the absence of spin-orbit coupling (SOC). The combination of spin-split bands and van-

ishing net macroscopic magnetization makes this class of compensated magnets attractive for spintronics and quantum information applications [6, 7].

Experimentally established altermagnets, including MnTe [8, 9] and MnTe₂ [10, 11], CrSb [12–14], KV₂Se₂O [15] and RbV₂Te₂O [16], are mostly weakly or moderately correlated *d*-electron systems. Closely related odd-parity *p*-wave magnets have also been proposed and realized in non-collinear magnetic materials such as NiI₂ [17] and Gd₃(Ru_{1- δ} Rh _{δ})₄Al₁₂ [18], though direct spectroscopic evidence remains elusive. In the spectroscopically established cases, the spin-split band structure is largely understood within a single-particle band theory governed by crystal and spin symmetries. Whether the same picture survives in strongly correlated environments, particularly *f*-electron heavy-fermion systems, is much less clear. In such systems, the low-energy electronic structure is governed by the Doniach competition [19]: the Ruderman–Kittel–Kasuya–Yosida (RKKY) interaction promotes long-range magnetic order, whereas Kondo correlations screen local moments and generate low energy *f*-derived quasiparticle spectral weight through *c*-*f* hybridization [20]. How this many-body competition modifies symmetry-allowed altermagnetic band splitting remains an open question.

CeNiAsO provides a concrete setting to address this question. It is an antiferromagnetic Kondo lattice with successive antiferromagnetic transitions at $T_{N1} \approx 9$ K and $T_{N2} \approx 6$ K - 7 K [21–23]. For its low-temperature coplanar magnetic phase, density functional theory (DFT) based calculations predict an odd-parity exchange splitting on the itinerant conduction bands, making CeNiAsO a candidate for metallic *p*-wave magnetism [24, 25]. Here we refer to this odd-parity compensated magnetic state more broadly as *p*-wave altermagnetism, and focus on its expected single-particle signature: a momentum-dependent *p*-wave exchange splitting of the itinerant bands. Recent transport measurements have reported a large field-trained in-plane resistivity anisotropy below T_{N2} [26], consistent with broken tetragonal symmetry in the magnetic ordered state. However, transport anisotropy does not directly determine whether the itinerant bands carry the anticipated single-particle exchange splitting. The microscopic manifestation of the predicted *p*-wave splitting in the electronic structure of CeNiAsO therefore remains to be clarified.

Here we use high-resolution laser-based angle-resolved photoemission spectroscopy (ARPES) to investigate the electronic structure of CeNiAsO across its magnetic transitions. We find no resolvable *p*-wave exchange splitting on the itinerant Ni *3d*-derived conduction bands:

the measured dispersions remain essentially unchanged upon entering the low-temperature ordered phase. By combining Fermi-surface mapping, orbital-resolved ARPES, resonant photoemission, and correlation-dependent DFT calculations, we show that the large splitting expected in an uncorrected itinerant- $4f$ picture is not the experimentally relevant band splitting. The measured Fermi surface is dominated by Ni $3d$ -derived itinerant bands and is inconsistent with the additional pockets produced by itinerant Ce $4f$ states at the calculated Fermi level. As a diagnostic comparison, evaluating the same itinerant- $4f$ calculation at the energy where the Ni $3d$ -derived Fermi-surface contours best match experiment gives only a much smaller residual splitting on the Ni $3d$ bands. Resonant ARPES further reveals weakly dispersive Ce $4f_{5/2}^1$ and $4f_{7/2}^1$ features, supporting a predominantly localized Ce $4f$ description with residual c - f hybridization. In the Schrieffer-Wolff picture [27], a large $4f$ Coulomb repulsion and a large $4f$ removal energy reduce the effective c - f exchange scale, providing a natural microscopic basis for why the p -wave splitting is barely transferred from the localized Ce moments to the itinerant Ni $3d$ bands. A localized- $4f$ DFT+ U treatment correspondingly removes the large $4f$ -dominated splitting from the experimentally relevant energy window and reduces the remaining Ni $3d$ -band splitting to the few-meV scale, comparable to the actual experimental broadening. Our results show that strong $4f$ correlations suppress the itinerant exchange splitting expected from a weak-correlation picture of p -wave magnetism, thereby challenging the conventional single-particle band picture in a heavy-fermion altermagnetic environment.

Results

CeNiAsO crystallizes in a tetragonal ZrCuSiAs-type structure (space group $P4/nmm$), where the Ce $4f$ moments form a coplanar noncollinear antiferromagnetic order (Fig. 1a). The corresponding Brillouin zone (BZ) and the (001) surface-projected BZ are shown in Fig. 1b. The high crystalline quality is confirmed by sharp Laue diffraction patterns on the (001) surfaces (see Supplementary Information). Macroscopic magnetization measurements reveal two successive magnetic phase transitions at $T_{N1} \approx 8.8$ K and $T_{N2} \approx 6.1$ K for the present crystals (Fig. 1c). The phase below T_{N2} is of particular theoretical interest because its coplanar magnetic structure has been proposed to realize a metallic p -wave magnetic state.

We first determine the Fermi-surface topology by combining synchrotron and laser ARPES measurements. Synchrotron measurements at $h\nu = 75$ eV (Fig. 1d) cover an extended momentum region and resolve the bulk-derived Fermi-surface contours (Fig. 1d), whereas the high-resolution ARPES at $h\nu = 7$ eV provide a detailed view of the near- E_F states around $\bar{\Gamma}$, where both surface and bulk contributions are visible (Fig. 1e). By tracking the band dispersions through the constant-energy contours, we extract the experimental Fermi surface contours summarized in Fig. 1f. The innermost near- $\bar{\Gamma}$ features are assigned to surface states, as supported by the CeO-terminated slab calculation shown later in Fig. 2. The CeO termination of the measured surface is identified from the termination-dependent Fermi-surface topology and work-function difference presented in the Supplementary Fig. S2. The remaining contours form the bulk itinerant manifold: three electron-like pockets (α , β_1 , and β_2) are centered at the \bar{M} point, while a hole-like pocket (γ) is centered at the \bar{X} point.

We then compare the measured Fermi-surface topology with first-principles calculations under different treatments of the Ce 4*f* electrons. When the Ce 4*f* states are included as valence electrons (Fig. 1g), the calculation yields extra Fermi-surface pockets that are absent in experiment, and therefore fails to reproduce the observed Fermi-surface topology. By contrast, when the Ce 4*f* states are treated as core-like and excluded from the valence electrons (Fig. 1h), the calculated Fermi surface matches the experimentally observed conduction-band pockets much more closely. This comparison suggests that the experimentally relevant Fermi surface is better described by a picture in which the Ce 4*f* electrons are largely localized, with the itinerant states arising predominantly from Ni 3*d* bands. The proposed *p*-wave exchange splitting should therefore be evaluated on these Ni 3*d*-derived conduction bands, motivating a more detailed orbital-resolved assignment using polarization-dependent ARPES.

ARPES spectra measured at $h\nu = 75$ eV provide an extended view of the bulk-derived band structure (Fig. 2a–c). Along the high-symmetry $\bar{\Gamma}$ – \bar{X} , $\bar{\Gamma}$ – \bar{M} , and \bar{X} – \bar{M} directions, the dominant dispersive features can be assigned to the bulk α , β_1 , β_2 , and γ pockets identified in Fig. 1. The overall dispersions are well reproduced by the nonmagnetic DFT band structure along the M – Γ – X – M path (Fig. 2f), confirming that the itinerant electronic structure is mainly derived from Ni 3*d* states.

We then use high-resolution laser ARPES at $h\nu = 7$ eV to resolve the near E_F bands in

greater detail (Fig. 2d,e). In this low-photon-energy regime, the spectral weight of the inner electron-like branch around $\bar{\Gamma}$ is strongly enhanced. Comparison with slab calculations for the CeO-terminated surface (Fig. 2g) supports the assignment of this branch to a surface state (SS), which is therefore separated from the bulk bands in the following analysis.

The orbital character of the bulk bands is further revealed by polarization-dependent ARPES. By switching the incident light polarization (*s*- and *p*-pol), initial states with different parities with respect to the experimental mirror plane are selectively enhanced. Along the $\bar{\Gamma}$ - \bar{X} direction (Fig. 2d), the bulk spectral weight is dominated by the γ band, whose polarization dependence is consistent with predominant Ni d_{yz} and d_{xy} character. Along the $\bar{\Gamma}$ - \bar{M} direction (Fig. 2e), the α , β_1 , and β_2 bulk bands are resolved together with the SS. The observed parity dependence supports an assignment of the α band mainly to $d_{x^2-y^2}$, d_{xz} , and d_{yz} components, while the $\beta_{1,2}$ bands are dominated by d_{z^2} and d_{xy} orbital characters. These assignments are consistent with the orbital-projected DFT results in Fig. 2f. For clarity, Fig. 2f shows only the dominant orbital component of each band; the full orbital-resolved projections are provided in the Supplementary Fig. S4.

With the paramagnetic band structure and Ni $3d$ orbital characters resolved, we next reassess the calculated *p*-wave exchange splitting under the experimental observation that the itinerant bands are predominantly Ni $3d$ -derived. This step is essential because, in the uncorrected itinerant- $4f$ calculation, the largest splitting originates from Ce $4f$ -derived bands near the calculated Fermi level, rather than from the experimentally observed Ni $3d$ conduction bands.

To directly probe the Ce $4f$ electronic structure, we performed resonant ARPES across the Ce $4d \rightarrow 4f$ resonance edge. Here, the experimentally accessible low-energy window refers to the energy range covered by our ARPES measurements, extending from E_F to approximately 1.2 eV below E_F . Figures 3a and 3b compare spectra measured along $\bar{\Gamma}$ - \bar{X} below resonance ($h\nu = 105$ eV) and on resonance ($h\nu = 120$ eV), respectively. At resonance, the spectra show a pronounced enhancement of nearly nondispersive Ce $4f$ -derived spectral weight. This is further highlighted in the second-derivative image of the on-resonance spectrum (Fig. 3c). The EDC comparison at $\bar{\Gamma}$ resolves the characteristic Ce $4f$ multiplet structure, including the near- E_F $4f_{5/2}^1$ resonance and the spin-orbit-split $4f_{7/2}^1$ satellite at $E - E_F \approx -0.28$ eV (Fig. 3d). In Ce-based resonant-photoemission studies, the deeper f^0 final-state feature associated with removal of a Ce $4f$ electron typically appears

at 1.5 - 2.5 eV below E_F , well below the $4f_{5/2}^1$ resonance and the $4f_{7/2}^1$ spin-orbit satellite near 0.28 - 0.30 eV [28, 29]. Its absence within the present near- E_F measurement window is consistent with a localized- $4f$ description in which the occupied Ce $4f$ removal spectral weight lies away from the Ni $3d$ -derived bands near E_F . These weakly dispersive resonant features support a predominantly localized Ce $4f$ description with residual c - f hybridization, rather than an ordinary itinerant- $4f$ band picture.

We then reassess the predicted p -wave splitting in light of the Ce $4f$ electronic structure revealed by resonant ARPES. In the $U_{\text{eff}} = 0$ calculation, the Ce $4f$ states are treated as valence states and contribute strongly near the Fermi level (Fig. 3e). At the unshifted calculated Fermi level, the itinerant Fermi surface contains additional Ce $4f$ -derived pockets that are not observed experimentally (Fig. 3h), indicating that the large splitting associated with these pockets is not directly relevant to the measured Fermi surface. To estimate the residual splitting on the experimentally observed Ni $3d$ -derived Fermi surface within this itinerant- $4f$ reference, we compare the calculated constant-energy contours with the ARPES Fermi surface in Fig. 1. The contour at $E_F^* = E_F - 0.25$ eV gives the closest match to the measured Ni $3d$ -derived pockets, and is therefore used as a rigid-band-aligned reference rather than as a model of an actual charge-doped state. At this E_F^* -aligned reference, the spin-polarized Fermi surface follows the experimentally observed Ni $3d$ -derived topology (Fig. 3f), and the corresponding band structure gives a residual p -wave splitting of ~ 10.3 meV on the Ni $3d$ -derived bands (Fig. 3g).

By contrast, the physically motivated treatment for a Ce-based Kondo lattice is obtained by including a strong on-site Coulomb interaction on the Ce $4f$ orbitals. For $U_{\text{eff}} = 6$ eV, the occupied Ce $4f$ spectral weight is shifted to higher binding energy, and its admixture with the Ni $3d$ -derived conduction bands is strongly reduced (Fig. 3i). The calculated itinerant Fermi surface in this localized- $4f$ treatment closely resembles the E_F^* -aligned $U_{\text{eff}} = 0$ reference and is dominated by Ni $3d$ -derived Fermi surface (Fig. 3j). The residual p -wave splitting on the Ni $3d$ -derived bands is further reduced to ~ 5.1 meV (Fig. 3k). Additional U_{eff} -dependent calculations show that, once the Ce $4f$ states are shifted away from the low-energy window, the residual Ni $3d$ -band splitting changes only weakly with U_{eff} and remains in the few-meV range (Supplementary Fig. S7).

These results are summarized in Fig. 3l. The uncorrected $U_{\text{eff}} = 0$ itinerant- $4f$ calculation gives a large Ce $4f$ -dominated splitting of ~ 50 meV and a Ni $3d$ -band splitting of ~ 14 meV.

However, this Fermi surface contains additional Ce $4f$ -derived pockets that are absent in experiment. When the same itinerant- $4f$ calculation is evaluated at the E_F^* -aligned reference that best matches the experimental Ni $3d$ Fermi surface, the residual Ni $3d$ -band splitting is reduced to ~ 10.3 meV. In the localized- $4f$ $U_{\text{eff}} = 6$ eV calculation, it is reduced further to ~ 5.1 meV, comparable to or below the actual 6.3 meV energy broadening of the high-resolution laser-ARPES measurements discussed below. Taken together, these comparisons show that the large $4f$ -dominated splitting of the uncorrected itinerant- $4f$ calculation is not the experimentally relevant splitting. When the Ce $4f$ states are treated consistently with the measured Fermi surface and their predominantly localized character, only a few-meV residual splitting remains on the Ni $3d$ -derived bands.

We now test this residual splitting directly using temperature-dependent ARPES. Synchrotron ARPES along Cut 1 tracks the band dispersion over a broad temperature range from the low-temperature ordered regime near 6.2 K to the paramagnetic state at 52 K (Fig. 4a). Within this temperature window, the main dispersive features remain essentially unchanged, with no obvious band reconstruction or additional folding associated with the magnetic transitions. This weak temperature dependence indicates that the overall conduction-band structure is not strongly reconstructed by the onset of magnetic order.

To search for more subtle changes on the Ni $3d$ -derived itinerant bands, we use high-resolution laser ARPES at $h\nu = 7$ eV to compare spectra taken below and above the magnetic transitions. The measured momentum cuts are shown in Fig. 4d. Cut 2 lies close to the $\bar{\Gamma}$ - \bar{X} direction, where the calculated residual p -wave splitting is expected to be most visible, while Cut 3 near $\bar{\Gamma}$ - \bar{M} provides a complementary reference direction. Figures 4b and 4c compare spectra measured at 1.6 K, inside the low-temperature commensurate Néel phase, and at 15 K, in the paramagnetic state. No additional band splitting or magnetic reconstruction is resolved in either cut.

This conclusion is further supported by the EDC and MDC comparisons in Figs. 4e and 4f. The spectra measured at 1.6 K and 15 K show nearly overlapping line shapes and peak positions within the experimental resolution. Thus, the anticipated p -wave exchange splitting is not resolved on the experimentally relevant Ni $3d$ -derived bands across the magnetic transitions. This absence is consistent with the theoretical reassessment in Fig. 3, where the residual Ni $3d$ -band splitting is reduced to the few-meV scale once the Ce $4f$ states are treated in a manner consistent with the experimental Fermi surface and resonant-ARPES

spectra.

Discussion and Conclusion

The coexistence of macroscopic signatures associated with the proposed p -wave magnetic order and the absence of a resolvable itinerant exchange splitting in CeNiAsO points to a regime in which p -wave antiferromagnetic symmetry and its single-particle band splitting signature become separated by strong $4f$ correlations. In a weak-correlation picture, the magnetic symmetry of a compensated magnet is expected to generate a momentum-dependent single-particle exchange splitting of the itinerant bands. Our ARPES results show that this correspondence breaks down in CeNiAsO: although the Ce moments undergo long-range magnetic ordering, the Ni $3d$ -derived conduction bands remain essentially unchanged across the successive magnetic transitions. The anticipated p -wave exchange splitting is therefore strongly suppressed in the experimentally accessible itinerant electronic structure.

This suppression is most directly understood by reassessing which part of the calculated splitting is relevant to the measured band structure. In the uncorrected itinerant- $4f$ calculation, the largest odd-parity splitting is carried by Ce $4f$ -derived bands near the calculated Fermi level. However, this same calculation produces additional $4f$ -derived Fermi-surface pockets that are not observed experimentally. The large $4f$ -dominated splitting in this weak-correlation limit therefore should not be directly compared with the measured Fermi surface. As a diagnostic tool within the same itinerant- $4f$ calculation, evaluating the band structure at the rigid-band-aligned reference E_F^* , where the calculated Ni $3d$ -derived Fermi-surface contours best match experiment, gives a much smaller residual splitting on the Ni $3d$ -derived bands.

The resonant ARPES results provide independent spectroscopic evidence on this interpretation. Resonant ARPES reveals the characteristic Ce $4f_{5/2}^1$ resonance near E_F , together with the spin-orbit-split $4f_{7/2}^1$ satellite at higher binding energy. This multiplet structure is widely recognized as a spectroscopic fingerprint of the Kondo-resonance channel in Ce-based heavy-fermion systems [28–30]. It shows that the localized Ce moments are not completely decoupled from the itinerant carriers; rather, a residual c - f hybridization remains active and provides the microscopic basis for Kondo screening and Kondo-lattice correlations. At the same time, the weak dispersion of the resonantly enhanced $4f$ -derived features supports a

predominantly localized Ce $4f$ description, rather than an ordinary itinerant- $4f$ band picture. This dual localized-and-hybridized character is precisely the regime expected for a Ce-based Kondo lattice.

The DFT+ U calculations then provide a microscopic description of this localized- $4f$ regime. In the uncorrelated magnetic calculation, the Ce $4f$ states remain itinerant near the Fermi level and generate a sizable odd-parity spin splitting, most prominently on the $4f$ -derived bands and, through hybridization, on the Ni $3d$ -derived conduction bands. Introducing a strong on-site Coulomb interaction on the Ce $4f$ orbitals shifts the occupied $4f$ spectral weight to higher binding energy and strongly reduces its low-energy admixture with the Ni $3d$ -derived bands. For $U_{\text{eff}} = 6$ eV, the residual Ni $3d$ -band splitting is reduced to ~ 5.1 meV, comparable to or below the actual experimental broadening of the laser-ARPES measurements. This conclusion does not rely on the precise value of U_{eff} : our U_{eff} -dependent calculations show that, once the Ce $4f$ states are shifted away from the conduction bands near E_F , the residual splitting on the Ni $3d$ -derived bands changes only weakly and remains in the few-meV range. The non-observation of a resolvable splitting therefore sets an experimental upper bound on the observable Ni $3d$ -band splitting, rather than uniquely determining a particular U_{eff} . It is nevertheless fully consistent with the localized- $4f$ description, in which strong Ce $4f$ correlations suppress the transfer of the symmetry-allowed p -wave exchange splitting to the measured Ni $3d$ -derived bands.

Importantly, the rigid-band comparison within the $U_{\text{eff}} = 0$ itinerant- $4f$ calculation should not be viewed as an alternative microscopic mechanism. It is a diagnostic test showing that the large calculated splitting is tied to $4f$ -derived states that do not form the experimentally observed Fermi surface. The DFT+ U calculation instead provides the physically motivated localized- $4f$ description appropriate for a Ce-based Kondo lattice. Both analyses point to the same experimentally relevant conclusion: the large $4f$ -dominated splitting does not correspond to the measured Fermi-surface topology; the remaining observable splitting is instead a small residual splitting on the Ni $3d$ -derived conduction bands.

This result challenges the simple single-particle expectation that a symmetry-allowed antiferromagnetic or p -wave magnetic order must necessarily produce a resolvable spin splitting on the measured low-energy bands. In CeNiAsO, magnetic order and itinerant quasiparticles are still coupled through residual c - f hybridization, but this coupling occurs in a strongly correlated $4f$ environment. The low-energy conduction electrons therefore do not experi-

ence the ordered Ce moments as a large static exchange field in the same way as in a weakly correlated altermagnet. Instead, the predominantly localized Ce $4f$ states strongly reduce the low-energy $4f$ admixture in the Ni $3d$ -derived bands near E_F , thereby suppressing the transfer of the symmetry-allowed p -wave exchange splitting to the experimentally accessible itinerant states. CeNiAsO thus realizes a correlation-driven suppression of altermagnetic band splitting rather than a conventional weak-correlation altermagnetic electronic structure.

This framework also reconciles our spectroscopic results with macroscopic transport observations. The reported in-plane resistivity anisotropy below T_{N2} is consistent with the broken rotational symmetry of the low-temperature magnetic state [26]. Our ARPES data indicate, however, that this anisotropy does not require a large Fermi-surface reconstruction or a resolvable static exchange splitting of the itinerant bands. A natural possibility is that the transport response is governed primarily by anisotropic scattering of itinerant quasiparticles from the symmetry-broken Ce magnetic sublattice, potentially enhanced by the momentum dependence of the residual c - f hybridization. Direct tests of this scattering-dominated scenario will require probes capable of resolving single magnetic domains and momentum-dependent quasiparticle lifetimes.

In conclusion, our high-resolution ARPES measurements reveal that the Ni $3d$ -derived bands in CeNiAsO do not develop a resolvable p -wave exchange splitting across the successive magnetic transitions. Fermi-surface mapping, resonant ARPES, and correlation-dependent first-principles calculations show that the large splitting predicted in an uncorrected itinerant- $4f$ picture is not the experimentally relevant band splitting. Instead, the measured Fermi surface and resonant $4f$ spectra support a predominantly localized Ce $4f$ description with residual Kondo-lattice hybridization, which reduces the observable Ni $3d$ -band splitting to the few-meV scale. CeNiAsO therefore provides a strongly correlated f -electron setting for p -wave altermagnetism, in which localized Ce $4f$ electrons suppress the observable single-particle band-splitting signature. More broadly, our results suggest that pressure, chemical substitution, and magnetic field may provide routes to tune the balance between $4f$ localization, Kondo-lattice hybridization, and momentum-dependent exchange splitting in correlated compensated magnetic systems.

Method

Single Crystal Growth and Characterization

High-quality CeNiAsO single crystals were grown using the self-flux method. Detailed macroscopic transport properties and additional crystalline-quality characterization of CeNiAsO single crystals have been reported previously [26]. The sample quality for the photoemission experiments was further verified *in situ* by core-level X-ray photoemission spectroscopy (XPS) [see Supplementary Information (SI)].

Angle-Resolved Photoemission Spectroscopy (ARPES)

ARPES measurements were carried out on three complementary setups to achieve comprehensive momentum and energy coverage. High-resolution data were acquired using two laboratory-based systems, both employing a 6.994 eV vacuum-ultraviolet (VUV) laser as the excitation source. On one of these systems, a -95 V bias was applied to the sample to extend the accessible in-plane momentum range [31]; the overall energy resolution was better than 8 meV and the momentum resolution was better than 0.01 \AA^{-1} . The second laser-based setup, configured for ultra-low-temperature operation, delivered an energy resolution of 6.3 meV, as determined from the Fermi edge of polycrystalline Au at 1.6 K. The lowest sample temperature reached 1.6 K in the high-resolution laser-ARPES measurements, well below the magnetic transition temperatures. Wider Brillouin-zone mapping and photon-energy-dependent scans were performed at the BL03U endstation of the Shanghai Synchrotron Radiation Facility (SSRF) [32], equipped with a Scienta Omicron DA30L hemispherical analyzer. Synchrotron data were taken at a photon energy of 75 eV with linear horizontal polarization, using a pass energy of 10 eV and a slit width of 0.3 mm. All samples were cleaved *in situ* in an ultra-high vacuum better than 4×10^{-11} mbar. Photon-energy-dependent measurements yielded an inner potential $V_0 = 16$ eV, placing the 75 eV data close to the bulk $k_z = 0$ (Γ) plane.

First-principles calculations

First-principles calculations were performed within density functional theory (DFT) using the projector augmented-wave (PAW) method, as implemented in the Vienna ab initio Simulation Package (VASP). The generalized-gradient approximation (GGA) in the Perdew–Burke–Ernzerhof (PBE) form was adopted for the exchange-correlation functional. The experimental crystal structure of CeNiAsO was used as the structural input. A plane-wave kinetic-energy cutoff of 520 eV was used for the main DFT+ U calculations, while a cutoff of 460 eV was applied for the plain PBE reference calculations without a Hubbard U . The electronic energy convergence criterion was set to 10^{-6} eV for the DFT+ U iterations and 10^{-5} eV for the PBE references.

To obtain a clean itinerant-band reference, non-magnetic calculations were performed using a specialized Ce PAW potential that suppresses explicit Ce $4f$ valence states. For calculations involving magnetic Ce $4f$ moments, the standard Ce PAW potential was employed using a commensurate noncollinear magnetic supercell. Spatial symmetries were explicitly disabled to allow for general magnetic configurations. In the plain PBE magnetic reference calculations, the Ce magnetic moments were constrained to the coplanar configuration associated with the low-temperature commensurate magnetic structure using a penalty functional approach. The target Ce magnetic moments for the four sublattices were constrained using the following spin matrix:

$$\mathbf{M}_{\text{Ce}} = \begin{pmatrix} 0.66 & -0.44 & 0 \\ -0.66 & -0.44 & 0 \\ -0.66 & 0.44 & 0 \\ 0.66 & 0.44 & 0 \end{pmatrix} \mu_{\text{B}}$$

in Cartesian coordinates. These constrained calculations provided an itinerant-limit reference to evaluate the specific impact of Ce $4f$ localization.

The on-site Coulomb interaction of the Ce $4f$ shell was treated using the rotationally invariant Dudarev DFT+ U formalism. The Hubbard correction was applied exclusively to the Ce $4f$ orbitals. To systematically examine the correlation dependence of the electronic structure, an extensive scan of the effective interaction was performed with $U_{\text{eff}} = 1, 2, 3, 4, 5,$ and 6 eV. The results of this systematic spin-polarized band evolution are detailed in the Supplementary Fig. S7. Furthermore, to establish a theoretical reference for the itinerant

conduction band structure, we also calculated the non-magnetic constant energy contours at $E - E_F = 0, -0.1, -0.2, -0.3,$ and -0.4 eV (provided in the SI), which serve as a direct theoretical counterpart to the ARPES mappings in Fig. 1. For the main text discussion, $U_{\text{eff}} = 6$ eV is used as a representative localized-4*f* calculation, while the U_{eff} -dependent results in Supplementary Fig. S7 show that the residual Ni 3*d*-band splitting remains in the few-meV range throughout the localized-4*f* regime.

Spin-orbit coupling (SOC) was included self-consistently in the noncollinear magnetic calculations. The spin expectation values were evaluated in the global spin frame, and the color scales in the spin-polarized band plots represent the expectation value of the out-of-plane spin component (S_z). Orbital-resolved band structures and densities of states were obtained by weighting the Kohn-Sham eigenvalues with the corresponding orbital projection coefficients.

To evaluate the fine details of the Fermi surface and generate smooth S_z spin-polarization maps, tight-binding models were constructed. Maximally localized Wannier functions were generated using Wannier90, utilizing spinor Wannier functions for the magnetic and SOC calculations. The projection basis comprised Ce 4*f*, Ni 3*d*, As 4*p*, and O 2*p* orbitals. The validity of the resulting Wannier Hamiltonians was checked by benchmarking the interpolated bands against the initial DFT dispersions within the low-energy window relevant to our ARPES measurements.

Surface states were calculated using symmetric Ce–O and Ni–As terminated slabs with ~ 21.7 Å vacuum. Nonmagnetic SOC slab bands were computed along Γ –X–M– Γ using the Ce₃ PAW potential. Surface character was evaluated from VASP PROCAR by projecting onto the outermost Ce atoms for the Ce–O slab and the outermost Ni/As atoms for the Ni–As slab.

Acknowledgement

This work is supported by the National Natural Science Foundation of China (Grant Nos. 12488201 by X.J.Z., 12374066 by L.Z. and 12374154 by X.T.L.), the National Key Research and Development Program of China (Grant Nos. 2021YFA1401800 by X.J.Z., 2022YFA1604200 by L.Z., 2022YFA1403900 by G.D.L. and 2023YFA1406000 by X.T.L.), CAS Superconducting Research Project (Grant No. SCZX-0101), Innovation Program for Quantum Science and Technology (Grant No. 2021ZD0301800 by X.J.Z.), the Youth Innovation Promotion Association of CAS (Grant No. Y2021006 by L.Z.) and the Synergetic Extreme Condition User Facility (SECUF).

H.W. acknowledges support from the National Natural Science Foundation of China (Grant No. 12188101), the National Key Research and Development Program of China (Grant No. 2022YFA1403800), and the New Cornerstone Science Foundation through the XPLOER PRIZE.

S.L.L. acknowledges support from the National Key Research and Development Program of China (Grant Nos. 2022YFA1403400 and 2021YFA1400400).

Author Contributions

X.J.Z., L.Z., S.L.L and J.X.Z. proposed and designed the research. J.X.Z and J.M.S. carried out the ARPES experiments. H.L.Z. and B.L. grew the single crystals. D.W., H.Z.G., W.J.M, H.R.D., Y.X., Y.H.L., Z.L.C., T.M.M., B.L., W.P.Z., N.C., M.K.X., J.Q.C., C.H.D., S.J.Z., Z.M.W., F.F.Z., F.Y., Q.J.P., Z.Y.X., G.D.L., X.T.L., H.Q.M., L.Z. and X.J.Z. contributed to the development and maintenance of the ARPES systems and related software development. X.M., Z.T.L., and M.Y. provided the experimental support for the measurements performed on BL03U in SSRF. Y.Y.S and H.M.W. contributed to theoretical analysis. X.J.Z., L.Z. and J.X.Z. analyzed the data and wrote the paper. All authors participated in discussions and comments on the paper.

-
- [1] L. Šmejkal, J. Sinova, and T. Jungwirth, Beyond Conventional Ferromagnetism and Antiferromagnetism: A Phase with Nonrelativistic Spin and Crystal Rotation Symmetry, *Physical Review X* **12**, 031042 (2022).

- [2] L. Šmejkal, J. Sinova, and T. Jungwirth, Emerging Research Landscape of Altermagnetism, *Physical Review X* **12**, 040501 (2022).
- [3] I. Mazin and The PRX Editors, Editorial: Altermagnetism—A New Punch Line of Fundamental Magnetism, *Physical Review X* **12**, 040002 (2022).
- [4] T. Jungwirth, J. Sinova, R. M. Fernandes, Q. Liu, H. Watanabe, S. Murakami, S. Nakatsuji, and L. Šmejkal, Symmetry, microscopy and spectroscopy signatures of altermagnetism, *Nature* **649**, 837 (2026).
- [5] Y. Liu, X. Chen, Y. Yu, J. Etxebarria, J. M. Perez-Mato, and Q. Liu, Symmetry classification of magnetic orders using oriented spin space groups, *Nature* **652**, 869 (2026).
- [6] T. Jungwirth, J. Sinova, P. Wadley, D. Kriegner, H. Reichlova, F. Krizek, H. Ohno, and L. Smejkal, Altermagnetic spintronics (2025), arXiv:2508.09748.
- [7] C. Li, J.-X. Hou, F.-C. Zhang, S.-B. Zhang, and L.-H. Hu, Spin-Polarized Josephson Supercurrent in Nodeless Altermagnets, *Physical Review Letters* **136**, 116701 (2026), arXiv:2509.13838.
- [8] J. Krempaský, L. Šmejkal, S. W. D’Souza, M. Hajlaoui, G. Springholz, K. Uhlířová, F. Alarab, P. C. Constantinou, V. Strocov, D. Usanov, W. R. Pudelko, R. González-Hernández, A. Birk Hellenes, Z. Jansa, H. Reichlová, Z. Šobáň, R. D. Gonzalez Betancourt, P. Wadley, J. Sinova, D. Kriegner, J. Minár, J. H. Dil, and T. Jungwirth, Altermagnetic lifting of Kramers spin degeneracy, *Nature* **626**, 517 (2024).
- [9] S. Lee, S. Lee, S. Jung, J. Jung, D. Kim, Y. Lee, B. Seok, J. Kim, B. G. Park, L. Šmejkal, C.-J. Kang, and C. Kim, Broken Kramers Degeneracy in Altermagnetic MnTe, *Physical Review Letters* **132**, 036702 (2024).
- [10] L.-D. Yuan, Z. Wang, J.-W. Luo, and A. Zunger, Prediction of low-Z collinear and noncollinear antiferromagnetic compounds having momentum-dependent spin splitting even without spin-orbit coupling, *Physical Review Materials* **5**, 014409 (2021).
- [11] Y.-P. Zhu, X. Chen, X.-R. Liu, Y. Liu, P. Liu, H. Zha, G. Qu, C. Hong, J. Li, Z. Jiang, X.-M. Ma, Y.-J. Hao, M.-Y. Zhu, W. Liu, M. Zeng, S. Jayaram, M. Lenger, J. Ding, S. Mo, K. Tanaka, M. Arita, Z. Liu, M. Ye, D. Shen, J. Wrachtrup, Y. Huang, R.-H. He, S. Qiao, Q. Liu, and C. Liu, Observation of plaid-like spin splitting in a noncoplanar antiferromagnet, *Nature* **626**, 523 (2024).
- [12] S. Reimers, L. Odenbreit, L. Šmejkal, V. N. Strocov, P. Constantinou, A. B. Hellenes, R. Jaeschke Ubierno, W. H. Campos, V. K. Bharadwaj, A. Chakraborty, T. Denneulin, W. Shi,

- R. E. Dunin-Borkowski, S. Das, M. Kläui, J. Sinova, and M. Jourdan, Direct observation of altermagnetic band splitting in CrSb thin films, *Nature Communications* **15**, 2116 (2024).
- [13] S. Santhosh, P. Corbae, W. J. Yáñez-Parreño, S. Ghosh, C. J. Jensen, A. V. Fedorov, M. Hashimoto, D. Lu, J. A. Borchers, A. J. Grutter, T. R. Charlton, S. Islam, D. Golovanova, Y. Zhao, A. Tauraso, A. Richardella, B. Yan, K. A. Mkhoyan, C. J. Palmstrøm, Y. Ou, and N. Samarth, Altermagnetic Band Splitting in 10 nm Epitaxial CrSb Thin Films, *Advanced Materials* **37**, e08977 (2025).
- [14] G. Yang, Z. Li, S. Yang, J. Li, H. Zheng, W. Zhu, Z. Pan, Y. Xu, S. Cao, W. Zhao, A. Jana, J. Zhang, M. Ye, Y. Song, L.-H. Hu, L. Yang, J. Fujii, I. Vobornik, M. Shi, H. Yuan, Y. Zhang, Y. Xu, and Y. Liu, Three-dimensional mapping of the altermagnetic spin splitting in CrSb, *Nature Communications* **16**, 1442 (2025).
- [15] B. Jiang, M. Hu, J. Bai, Z. Song, C. Mu, G. Qu, W. Li, W. Zhu, H. Pi, Z. Wei, Y.-J. Sun, Y. Huang, X. Zheng, Y. Peng, L. He, S. Li, J. Luo, Z. Li, G. Chen, H. Li, H. Weng, and T. Qian, A metallic room-temperature d-wave altermagnet, *Nature Physics* **21**, 754 (2025).
- [16] F. Zhang, X. Cheng, Z. Yin, C. Liu, L. Deng, Y. Qiao, Z. Shi, S. Zhang, J. Lin, Z. Liu, M. Ye, Y. Huang, X. Meng, C. Zhang, T. Okuda, K. Shimada, S. Cui, Y. Zhao, G.-H. Cao, S. Qiao, J. Liu, and C. Chen, Crystal-symmetry-paired spin–valley locking in a layered room-temperature metallic altermagnet candidate, *Nature Physics* **21**, 760 (2025).
- [17] Q. Song, S. Stavrić, P. Barone, A. Droghetti, D. S. Antonenko, J. W. F. Venderbos, C. A. Occhialini, B. Ilyas, E. Ergeçen, N. Gedik, S.-W. Cheong, R. M. Fernandes, S. Picozzi, and R. Comin, Electrical switching of a p-wave magnet, *Nature* **642**, 64 (2025).
- [18] R. Yamada, M. T. Birch, P. R. Baral, S. Okumura, R. Nakano, S. Gao, M. Ezawa, T. Nomoto, J. Masell, Y. Ishihara, K. K. Kolincio, I. Belopolski, H. Sagayama, H. Nakao, K. Ohishi, T. Ohhara, R. Kiyanagi, T. Nakajima, Y. Tokura, T.-h. Arima, Y. Motome, M. M. Hirschmann, and M. Hirschberger, A metallic p-wave magnet with commensurate spin helix, *Nature* **646**, 837 (2025).
- [19] S. Doniach, The Kondo lattice and weak antiferromagnetism, *Physica B+C* **91**, 231 (1977).
- [20] Q. Si and F. Steglich, Heavy Fermions and Quantum Phase Transitions, *Science* **329**, 1161 (2010).
- [21] Y. Luo, H. Han, H. Tan, X. Lin, Y. Li, S. Jiang, C. Feng, J. Dai, G. Cao, Z. Xu, and S. Li, CeNiAsO: An antiferromagnetic dense Kondo lattice, *Journal of Physics: Condensed Matter*

- 23**, 175701 (2011).
- [22] Y. Luo, L. Pourovskii, S. E. Rowley, Y. Li, C. Feng, A. Georges, J. Dai, G. Cao, Z. Xu, Q. Si, and N. P. Ong, Heavy-fermion quantum criticality and destruction of the Kondo effect in a nickel oxypnictide, *Nature Materials* **13**, 777 (2014).
- [23] S. Wu, W. A. Phelan, L. Liu, J. R. Morey, J. A. Tutmaher, J. C. Neuefeind, A. Huq, M. B. Stone, M. Feyngenson, D. W. Tam, B. A. Frandsen, B. Trump, C. Wan, S. R. Dunsiger, T. M. McQueen, Y. J. Uemura, and C. L. Broholm, Incommensurate Magnetism Near Quantum Criticality in CeNiAsO, *Physical Review Letters* **122**, 197203 (2019).
- [24] A. B. Hellenes, T. Jungwirth, R. Jaeschke-Ubiergo, A. Chakraborty, J. Sinova, and L. Šmejkal, P-wave magnets (2024), arXiv:2309.01607.
- [25] A. Chakraborty, A. Birk Hellenes, R. Jaeschke-Ubiergo, T. Jungwirth, L. Šmejkal, and J. Sinova, Highly efficient non-relativistic Edelstein effect in nodal p-wave magnets, *Nature Communications* **16**, 7270 (2025).
- [26] H. Zhou, M. Wang, X. Ma, G. Li, D.-F. Shao, B. Liu, and S. Li, Anisotropic resistivity of a p-wave magnet candidate CeNiAsO (2025), arXiv:2509.07351.
- [27] J. R. Schrieffer and P. A. Wolff, Relation between the Anderson and Kondo Hamiltonians, *Physical Review* **149**, 491 (1966).
- [28] S.-i. Fujimori, A. Fujimori, K. Shimada, T. Narimura, K. Kobayashi, H. Namatame, M. Taniguchi, H. Harima, H. Shishido, S. Ikeda, D. Aoki, Y. Tokiwa, Y. Haga, and Y. Ōnuki, Direct observation of a quasiparticle band in CeIrIn₅: An angle-resolved photoemission spectroscopy study, *Physical Review B* **73**, 224517 (2006).
- [29] S. Patil, A. Generalov, M. Güttler, P. Kushwaha, A. Chikina, K. Kummer, T. C. Rödel, A. F. Santander-Syro, N. Caroca-Canales, C. Geibel, S. Danzenbächer, Yu. Kucherenko, C. Laubschat, J. W. Allen, and D. V. Vyalikh, ARPES view on surface and bulk hybridization phenomena in the antiferromagnetic Kondo lattice CeRh₂Si₂, *Nature Communications* **7**, 11029 (2016).
- [30] Q. Y. Chen, D. F. Xu, X. H. Niu, J. Jiang, R. Peng, H. C. Xu, C. H. P. Wen, Z. F. Ding, K. Huang, L. Shu, Y. J. Zhang, H. Lee, V. N. Strocov, M. Shi, F. Bisti, T. Schmitt, Y. B. Huang, P. Dudin, X. C. Lai, S. Kirchner, H. Q. Yuan, and D. L. Feng, Direct observation of how the heavy-fermion state develops in CeCoIn₅, *Physical Review B* **96**, 045107 (2017).
- [31] T. Miao, Y. Xu, B. Liang, W. Zhu, N. Cai, M. Xu, D. Wu, H. Gu, W. Mao, S. Zhang,

- F. Zhang, F. Yang, Z. Wang, Q. Peng, Z. Xu, Z. Zhu, X. Li, H. Mao, L. Zhao, G. Liu, and X. J. Zhou, Expansion of momentum space and full 2π solid angle photoelectron collection in laser-based angle-resolved photoemission spectroscopy by applying sample bias, *Review of Scientific Instruments* **97**, 033908 (2026).
- [32] Y.-C. Yang, Z.-T. Liu, J.-S. Liu, Z.-H. Liu, W.-L. Liu, X.-L. Lu, H.-P. Mei, A. Li, M. Ye, S. Qiao, and D.-W. Shen, High-resolution ARPES endstation for in situ electronic structure investigations at SSRF, *Nuclear Science and Techniques* **32**, 31 (2021).

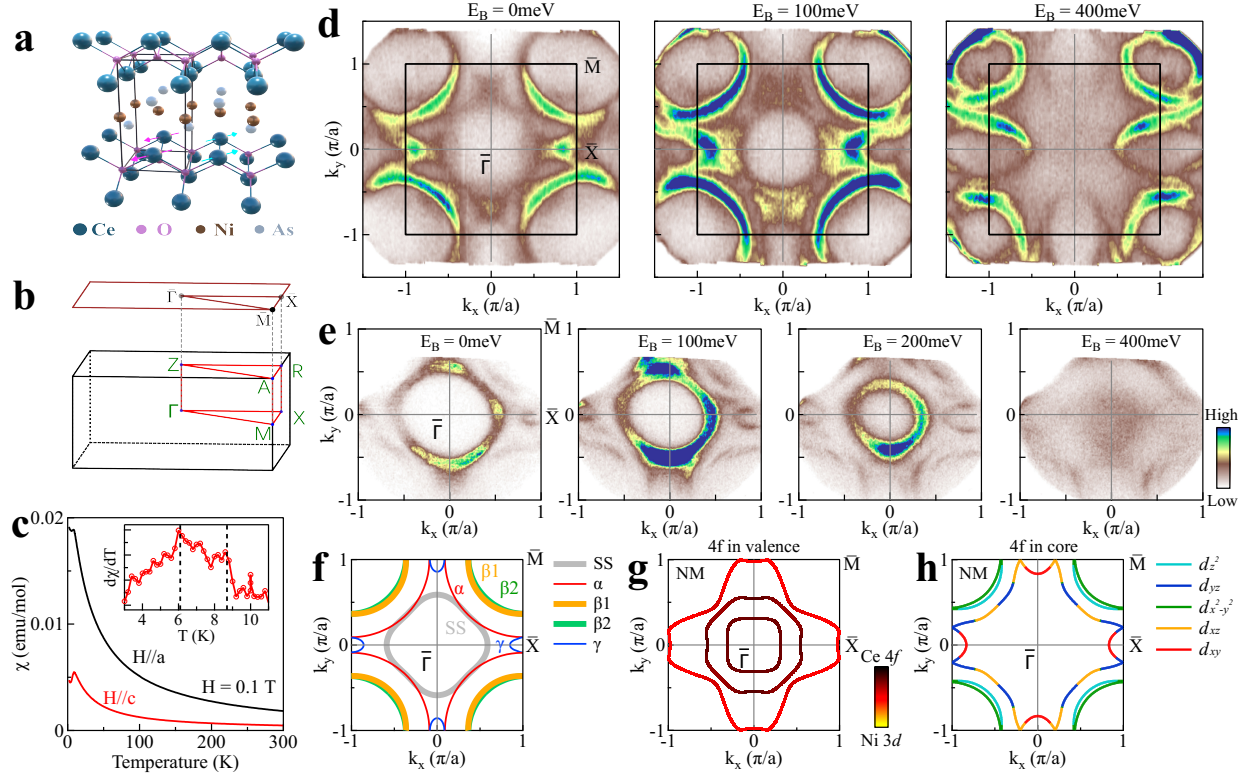


FIG. 1. **Single-crystal characterization and itinerant electronic structure of CeNiAsO.** (a) Crystal structure of CeNiAsO. The staggered Ce moments are indicated by arrows. (b) Three-dimensional bulk Brillouin zone (BZ) and the corresponding (001) surface-projected BZ, with high-symmetry points indicated. (c) Temperature dependence of the magnetic susceptibility χ measured under $H = 0.1$ T for fields applied parallel and perpendicular to the c axis. The inset shows $d\chi/dT$, resolving the two successive magnetic transitions. (d) Constant-energy contours measured by synchrotron ARPES at $h\nu = 75$ eV for binding energies $E_B = 0, 100$ and 400 meV. The black rectangle marks the surface-projected first BZ. (e) Corresponding high-resolution laser-ARPES constant-energy contours measured at $h\nu = 7$ eV for $E_B = 0, 100, 200$ and 400 meV, highlighting the near- $\bar{\Gamma}$ states. (f) Experimental Fermi-surface contours extracted from the 75 eV ARPES constant-energy maps. The inner contour is assigned to the surface state (SS), while the $\alpha, \beta_1, \beta_2,$ and γ contours denote bulk-derived bands used to establish the itinerant-band reference. (g), (h) Fermi surfaces from nonmagnetic density-functional-theory (DFT) calculations with Ce 4f electrons treated as valence and core states, respectively.

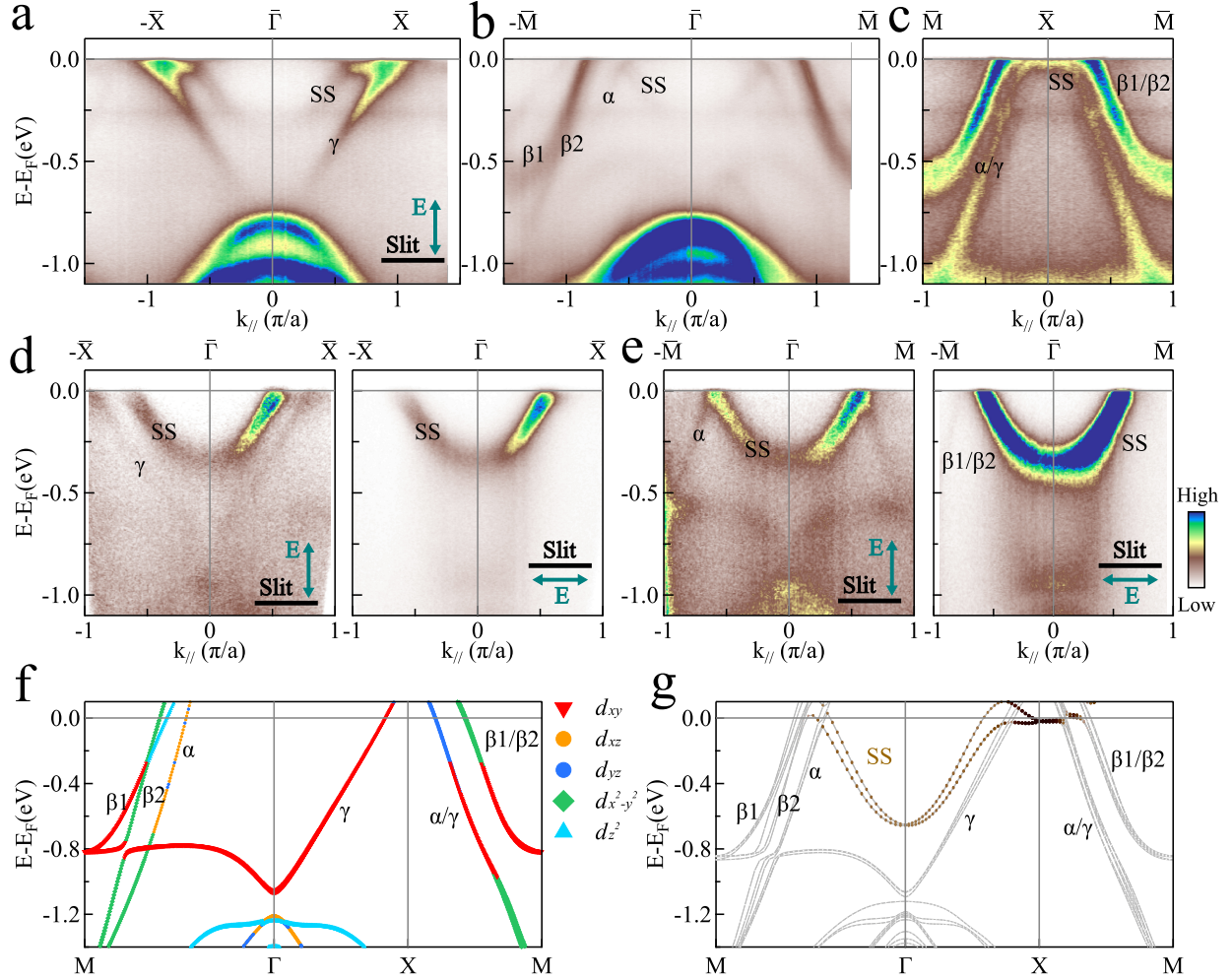


FIG. 2. **Orbital character and surface-state contribution in the electronic structure of CeNiAsO.** (a)-(c) ARPES spectra measured at $h\nu = 75$ eV along the high-symmetry $\bar{X}-\bar{\Gamma}-\bar{X}$, $\bar{M}-\bar{\Gamma}-\bar{M}$, and $\bar{M}-\bar{X}-\bar{M}$ directions, respectively. The main bulk-derived bands are labelled as α , $\beta_{1,2}$, and γ , while the near- $\bar{\Gamma}$ branch is assigned to a surface state (SS). (d)-(e) Polarization-dependent laser-ARPES spectra measured at $h\nu = 7$ eV along $\bar{X}-\bar{\Gamma}-\bar{X}$ and $\bar{M}-\bar{\Gamma}-\bar{M}$, respectively. The comparison between s - and p -polarized geometries resolves the parity dependence of the observed bands. (f) Nonmagnetic orbital-projected DFT band structure (Ce $4f$ electrons in core state) along the $M-\Gamma-X-M$ path. The dominant Ni-3d orbital characters are indicated by colors and symbols. (g) Slab calculation along the same momentum path. The surface-projected spectral weight identifies the strongly enhanced near- $\bar{\Gamma}$ branch observed in the laser-ARPES spectra as a surface-state contribution, separating it from the bulk itinerant bands used for the analysis of the p -wave exchange splitting.



FIG. 3. **Spectroscopic evidence on Ce 4f states and reassessment of the calculated p -wave exchange splitting.** (a), (b) ARPES spectra measured along $\bar{\Gamma}\text{-}\bar{X}$ below ($h\nu = 105$ eV) and on ($h\nu = 120$ eV) the Ce $4d \rightarrow 4f$ resonance edge, respectively. (c) Second-derivative image of the on-resonance spectrum in (b), highlighting the nearly nondispersive Ce $4f$ -derived multiplets. (d) Comparison of EDCs extracted at $\bar{\Gamma}$, revealing the resonant enhancement of the $4f_{5/2}^1$ state near the Fermi level (E_F) and the spin-orbit excited $4f_{7/2}^1$ state bound at -0.28 eV. (e) Calculated altermagnetic band structure for $U_{\text{eff}} = 0$, with color indicating the relative Ce $4f$ and Ni $3d$ orbital weights. $E_F^* = E_F - 0.25$ eV denotes the rigid-band-aligned reference at which the calculated Ni $3d$ -derived Fermi-surface contours best match experiment. (f) Spin-polarized Fermi surface of the $U_{\text{eff}} = 0$ calculation evaluated at E_F^* . (g) Spin-polarized band structure, showing the residual p -wave splitting on the Ni $3d$ -derived bands. (h) Calculated Fermi surface in the altermagnetic state at the unshifted E_F , showing additional Ce $4f$ -derived pockets. DFT+U ($U_{\text{eff}} = 6$ eV) calculated altermagnetic (i) band structure with orbital projection, (j) Fermi surface and (k) spin-projected bands, where the residual p -wave splitting in the Ni $3d$ bands is reduced. (l) Summary of the calculated spin splitting magnitudes on Ce $4f$ - or Ni $3d$ -derived bands at different energy (E_F or E_F^*) under different U_{eff} (0 or 6 eV) treatments of the Ce $4f$ states.

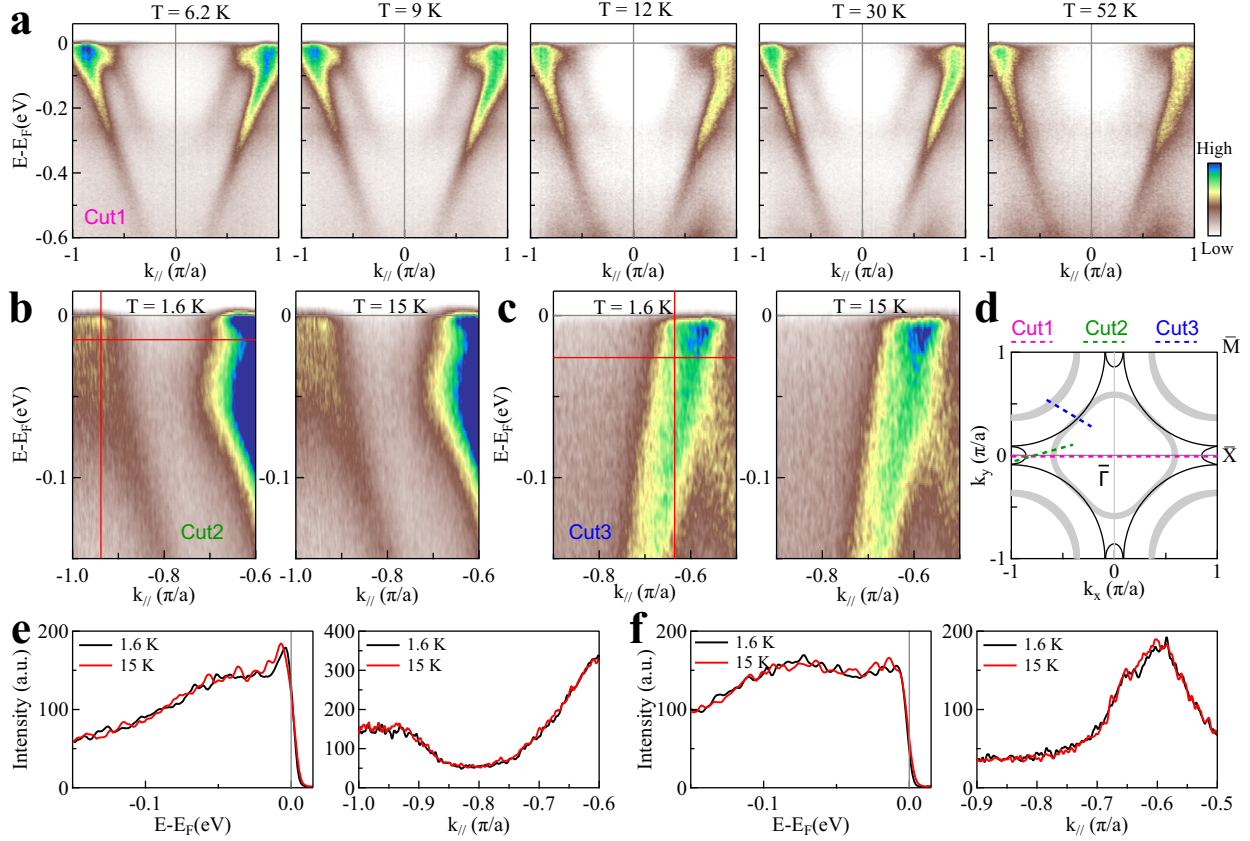


FIG. 4. Absence of resolvable low-energy exchange splitting across the successive magnetic transitions. (a) Temperature-dependent ARPES spectra measured along Cut 1, as defined in panel (d), from the low-temperature magnetic phase to the paramagnetic phase. The overall band dispersion remains essentially unchanged between 6.2 K and 52 K. (b),(c) High-resolution laser-ARPES spectra measured at $h\nu = 7$ eV at 1.6 K and 15 K along Cut 2 and Cut 3, respectively. Cut 2 probes the itinerant bands where the anticipated p -wave exchange splitting is expected to be most visible and Cut 3 provides a complementary reference direction. The red lines mark the representative energy and momentum positions used for the EDC and MDC comparisons. (d) Schematic Fermi-surface map showing the momentum locations of Cut 1, Cut 2, and Cut 3. (e)–(f) Direct comparison of EDCs and MDCs extracted from the 1.6 K and 15 K spectra in panels (b) and (c), respectively. The nearly overlapping spectral profiles indicate that no resolvable temperature-dependent exchange splitting or band reconstruction develops in the measured itinerant bands upon entering the commensurate Néel phase.